Method for reversing the laser modulation in a storage ring

Weihang Liu, Yu Zhao, Xiao Li,* and Sheng Wang†
Institute of High Energy Physics, Chinese Academy of Sciences, Beijing 100049, China
and Spallation Neutron Source Science Center, Dongguan 523803, China

Yi Jiao‡
Institute of High Energy Physics, Chinese Academy of Sciences, Beijing 100049, China

Chao Feng
Shanghai Institute of Applied Physics, Chinese Academy of Sciences, Shanghai 201800, China
and Shanghai Advanced Research Institute, Chinese Academy of Sciences, Shanghai 201210, China

(Received 3 November 2024; accepted 3 June 2025; published 27 June 2025)

The pursuit of coherent radiation generation remains a key direction in the advancement of storage ring light sources. Despite the potential of laser modulation in achieving this goal, it leads to a significant decline in the quality of the electron beam. Efforts to mitigate this decline have resulted in the proposal of demodulation schemes. However, implementing modulation and demodulation within the storage ring presents significant challenges due to dynamical and spatial constraints within straight sections. In this study, we propose a straightforward and easily implementable method for achieving reversible laser modulation in a storage ring. Notably, our approach circumvents the need for lengthy straight sections or bypass section. Simulation results show a substantial restoration of beam quality following demodulation. This innovative scheme holds great promise for the realization of high repetition rate coherent storage ring light sources.

DOI: 10.1103/rlt4-8bn9

I. INTRODUCTION

As a crucial experimental tool for scientific inquiry, the performance of light sources continues to evolve in tandem with scientific progress. Notably, particle accelerator-based light sources are continually advancing their technology and capabilities to meet the demands of scientific exploration. The free electron laser (FEL) exemplifies this progression, transitioning from normal conducting accelerators to superconducting accelerators. This upgrade has significantly increased the repetition rate of radiation pulses by nearly 5 orders of magnitude [1]. Furthermore, leveraging sophisticated beam manipulation techniques, FELs now offer temporal resolutions on the scale of attoseconds [2], empowering attosecond science with an unparalleled tool [3].

Similarly, the storage ring light source (SRLS) has also undergone significant enhancements. By adopting the multibend achromat design [4], SRLS has achieved a substantial reduction in its natural emittance, approaching the diffraction limit of x-rays. Consequently, the brightness of the light source has surged by more than 2 orders of magnitude, heralding a new era of enhanced performance and capabilities.

The high repetition rate, multiuser capability, and high stability of SRLS make it more attractive than FEL. However, its longitudinal coherence and time resolution are still not comparable to FELs. At present, the time resolution of SRLS is basically in the picosecond range or longer. In addition, its energy resolution is also limited by the monochromator technology, which is difficult to break through to the millielectronvolt scale. These limitations have made it difficult to meet some of the needs of current and future scientific research, and it is therefore necessary to be improved.

The generation of microbunches via laser modulation represents a viable solution for fulfilling this requirement. By interacting the beam with a laser in an undulator (referred to as modulator), the beam is given an energy modulation. This energy modulation is converted to density modulation after the beam passes through a longitudinal dispersion section. This density modulated beam will

*Contact author: lixiao@ihep.ac.cn
†Contact author: wangs@ihep.ac.cn
‡Contact author: jiaoyi@ihep.ac.cn

Published by the American Physical Society under the terms of the Creative Commons Attribution 4.0 International license. Further distribution of this work must maintain attribution to the author(s) and the published article's title, journal citation, and DOI.

generate coherent radiation in the downstream undulator (referred to as radiator) at a high harmonic of the laser [5–10]. Due to the properties of coherent radiation, the radiated power is proportional to the square of the beam charge and the pulse duration is proportional to the modulated laser pulse duration. These properties are capable of generating radiation pulses with high power and variable duration.

By combining the "flat" nature of the storage ring, i.e., its ultralow vertical emittance, numerous laser modulation schemes better suited for the storage ring have been proposed. For instance, vertical momentum (or angular) modulation can be induced in the beam using a TEM01 or tilted incidence laser [11–14]. This modulation can then be converted into density modulation as the beam traverses through a dispersion section, benefiting from the ultralow vertical emittance, which significantly enhances the density modulation. Furthermore, energy modulation schemes can also benefit from the ultralow vertical emittance. One such method, called angular dispersion microbunching generation (ADM) [15], utilizes a dipole to couple the longitudinal and transverse motion of an electron prior to energy modulation. The resultant energy modulation is then converted into density modulation through a dogleg. This approach has been utilized in the design of a coherent radiation beamline within a straight section of a storage ring [16,17].

Regardless of the type of modulation, it inevitably affects the beam, leading to a degradation in beam quality. This degradation makes it challenging to modulate the beam continuously or at high frequencies, thus limiting the repetition rate. To address this issue, demodulation schemes have been proposed [18,19]. These schemes restore beam quality by demodulating the modulated beam.

The demodulation process for energy modulation is relatively straightforward compared to angular modulation, as it primarily involves removing the energy modulation. In contrast, angular modulation requires additional considerations, such as betatron motion in the vertical plane and precise matching of the beta function phase shift. Therefore, choosing an ADM modulation scheme makes it easier to design a demodulation transport. However, considering the complexity of the storage ring dynamics and the limited space of the straight sections, it is extremely challenging to design a reversible ADM within a single straight section of a storage ring. The main difficulty is to design an isochronous transport between energy modulation and demodulation. This requires sufficient space on the one hand and a delicate design on the other to avoid excessive impact on the storage ring dynamics.

There are two ways to handle this difficulty, one is by designing a dedicated long straight section storage ring [19]. The other is to place the reversible ADM in the bypass of the storage ring [18]. The bypass design requires frequent injection and extraction to achieve coherent radiation, and the technical constraints of the injection and extraction elements impose limitations on the achievable repetition rate. On the other hand, designing a dedicated long straight section is not a standard requirement for a typical SRLS. Additionally, the layout of the bypass and the long straight section can be designed to support a ring-based FEL [20–27], which could make the laser modulation-based coherent radiation methods less attractive.

To enable the implementation of a reversible ADM in a typical storage ring, this paper presents a simple scheme. In this approach, the ADM and the demodulation section are situated in distinct straight sections, while an isochronous transport is established using arc sections and a horizontal chicane positioned between the ADM and the demodulation sections. The feasibility of the scheme is verified through simulations based on the parameters of the Southern Advanced Photon Source (SAPS) [28]. Postmodulation, a microbunch structure is achievable, demonstrating sufficient capability for producing coherent radiation. Following demodulation, beam parameters are largely restored. After the beam passes the demodulation section and completes the ADM process, the lasers are turned off, allowing the beam to undergo damping in the ring for several turns. This process is followed by reactivating the lasers, thus repeating the cycle. Simulations suggest that approximately 600 turns of damping are necessary to achieve stable and optimal radiation performance. This means that coherent pulses appear in a burst mode. As shown in Fig. 1, a possible burst mode is illustrated. In this mode, coherent pulses are not generated uniformly but rather as a series containing the same number of pulses as the bunches. This coherent pulse train repeats every 600 turns, equivalent to a repetition rate of 0.25 MHz. The resulting average coherent radiation flux can reach 10^{15} photons/s, with a bandwidth of less than 10^{-4}. In contrast, under similar bandwidth conditions, the photon flux from synchrotron radiation is constrained to approximately 2.5×10^{13} photons/s, indicating a reduction of more than 1 order of magnitude compared to coherent radiation. This substantial enhancement underscores the potential of the proposed method for advancing new directions in the development of SRLS.

In the following sections, we will present detailed information regarding the proposed method, including a specific example demonstrated on SAPS in Sec. III. The repetition rate and radiation performance will be discussed in Sec. IV. Finally, based on these results, we will provide our discussion and conclusions in Sec. V.

II. REVERSIBLE ADM IMPLEMENTED IN STRAIGHT SECTIONS OF A STORAGE RING

To enhance the utilization of a storage ring for a given circumference, it is common practice to limit the length of

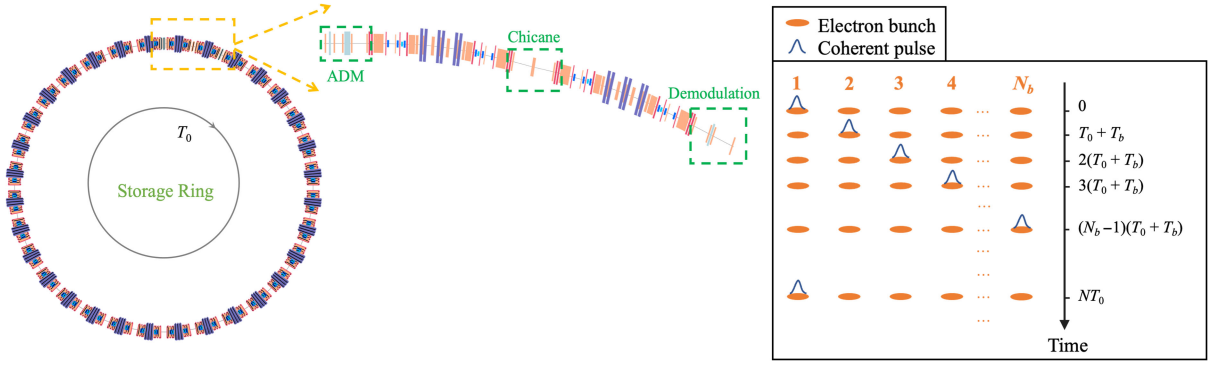


FIG. 1. Layout of a reversible ADM in a storage ring with a potential burst mode, where T_0 and T_b are the revolution time and the bunch spacing, respectively, and N is the number of turns required for the beam parameters to be restored. In this mode, the storage ring accommodates N_b bunches. Given that T_b is typically nanosecond-scale and the laser repetition rate is limited, the system must wait for each modulated bunch to complete one full revolution (or more) before modulating the next bunch (after an additional T_b delay). Consequently, following the first bunch modulation and initial coherent pulse generation, subsequent bunches are modulated at fixed intervals of $T_0 + T_b$. Once all N_b bunches are modulated, the cycle restarts from the first bunch if it has completed N turns and its beam parameters are restored. Otherwise, the system waits for $NT_0 - (N_b - 1)(T_0 + T_b)$ before resuming modulation.

straight sections to a relatively short range, typically 5–6 m. In order to achieve reversible ADM in such storage rings, it is necessary to place modulation and demodulation in separate straight sections. Typically, storage rings are multiperiod structures; for instance, the SAPS has a period of 32. In this configuration, the ADM section and the demodulation section are positioned in two separate straight sections, with a horizontal chicane situated between them in the third straight section, as illustrated in Fig. 1.

This layout enables the achievement of isochronous transport from the modulation section to the demodulation section. Following energy modulation in the ADM section, the beam proceeds through downstream components including a dogleg, radiator, and dipoles, contributing to the longitudinal dispersion $R_{56,\mathrm{adm}}$ in the isochronous transport. Subsequently, the beam traverses the first arc region after the ADM section to reach the horizontal chicane. It then passes through the second arc region to access the demodulation section. Within the demodulation section, the beam encounters two vertical dipoles before reaching the modulator, which also imparts longitudinal dispersion $R_{56,\mathrm{dem}}$. Summing all longitudinal dispersion contributions yields the total longitudinal dispersion of the isochronous transport, $R_{56,\mathrm{tot}} = R_{56,\mathrm{adm}} + 2R_{56,r} + R_{56,c} + R_{56,\mathrm{dem}}$, where $R_{56,r}$ and $R_{56,c}$ represent the arc and chicane longitudinal dispersion, respectively. Following the isochronous requirement, we obtain

$$\begin{aligned} R_{53,\mathrm{tot}} &= 0, \\ R_{54,\mathrm{tot}} &= 0, \\ R_{56,\mathrm{tot}} &= 0. \end{aligned} \tag{1}$$

The achievement of zero $R_{56,\mathrm{tot}}$ benefits from the fact that the longitudinal dispersion $R_{56,r}$ of a typical storage ring arc section is opposite in sign to the other contributing terms of $R_{56,\mathrm{tot}}$.

Given the ADM parameters and layout shown in Fig. 2, the isochronous requirement can be achieved by adjusting the deflection angle θ of the chicane dipoles, as well as the deflection angles θ_4 and θ_5 of the two dipoles upstream of the modulator in the demodulation section. It's worth noting that both the modulation and demodulation sections are located in straight sections, so $R_{51,\mathrm{tot}}$ and $R_{52,\mathrm{tot}}$ naturally become zero.

The ADM section needs to be designed to target the coherent radiation performance or the magnitude of the bunching factor for a particular harmonic. The ADM bunching factor for harmonic number n is related to the beam parameters as [15]:

$$b(n) = J_n(nk_L r_{56} A) \exp\left[-\frac{1}{2}(nk_L \eta)^2 \gamma_y \epsilon_y\right], \tag{2}$$

where r_{56} and η are the dogleg vertical and longitudinal dispersions of the ADM, respectively, A is the modulation amplitude, γ_y is the Twiss parameter of the ADM entrance in the vertical direction, ϵ_y is the vertical emittance, and k_L is the wave number of the laser.

Equation (2) indicates that the storage ring vertical emittance should be controlled at a relatively low level

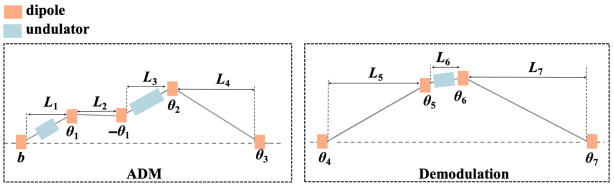


FIG. 2. Layout of the ADM and demodulation in straight sections.

to obtain a sufficiently large bunching factor. Since both the ADM section and the demodulation section contribute to the vertical dispersion, the dipoles, modulators, and radiator in both sections contribute to the quantum excitation, increasing the vertical emittance:

$$\epsilon_y \propto \int_{\text{dipole,mod ,rad}} \frac{H_y}{|\rho|^3} ds, \tag{3}$$

where H_y is the vertical chromatic H-function. The most effective way to reduce the growth of vertical emittance is to minimize the dispersion of these two sections.

The layout of the ADM section, as depicted in Fig. 2, consists of five dipoles, a modulator, and a radiator. To ensure achromatic conditions and coaxiality of the entrance and exit beams, the deflection angle and spacing of the dipoles must satisfy the following [29]:

$$\begin{aligned} &b\left(L_1+L_2+L_3+L_4+\frac{9L_b}{2}\right)+(L_2+L_b)\theta_1+\left(L_4+\frac{3}{2}L_b\right)\theta_2+\frac{1}{2}L_b\theta_3=0,\\ &b+\theta_2+\theta_3=0. \end{aligned} \tag{4}$$

Here, $b, \theta_1, -\theta_1, \theta_2, \theta_3$ correspond to the deflection angles of the first to the fifth dipole, L_i $(i = 1, 2, 3, 4)$ represents the distance between the dipoles, and L_b represents the length of each dipole.

Under these conditions, combined with the ADM optimality condition [15]

$$\begin{aligned} &r_{56}+b\eta=0,\\ &1+Ak_L r_{56}=0. \end{aligned} \tag{5}$$

It can be observed that the dispersion of the ADM section is positively correlated with the deflection angle b, and the bunching factor also shows a positive correlation with b, assuming a fixed vertical emittance. Therefore, there is a trade-off between low dispersion and a high bunching factor. Given the modulation strength, one can optimize the bunching factor to find deflection angle b or to choose a small enough one.

The demodulation section, as shown in Fig. 2, has a layout similar to that of the ADM section and comprises only four dipoles and a modulator. Once the parameters of the ADM section are defined, the parameters of the two dipoles preceding the modulator are exclusively determined by the isochronous condition [Eq. (1)]. Similarly, the parameters of the last two dipoles are determined by the achromatic and coaxial conditions.

The method described above facilitates the implementation of reversible ADM designs for typical storage rings. This approach is easier to construct and optimize compared to the scheme based on the lengthy straight section [19].

III. REVERSIBLE ADM BASED ON SAPS

To demonstrate the proposed scheme, we utilize the SAPS storage ring for reversible ADM design. It is worth noting that while this design may not be optimal, it sufficiently showcases the proposed approach. The SAPS storage ring operates at an energy of 3.5 GeV with a natural emittance of 33 pm and a straight section length of 6 m.

A. ADM and demodulation design

In the ADM section, we adopt an energy modulation amplitude of 0.14% and a laser wavelength of 266 nm. In practical operation, this wavelength can be fine-tuned, and the dipole strengths in the ADM, chicane, and demodulation sections can be adjusted to match the ADM and demodulation conditions. Additionally, the laser may be generated by a high-average-power fiber laser [30], which is potentially capable of delivering average power on the order of hundreds of kW [31].

Somewhat arbitrarily, the deflection angle of the first dipole in the ADM section is set to 5 mrad. Given the limited space available in the straight sections, the modulator has a period number of 1 with a length of 0.25 m. The radiator has a period number of 7 with a length of 0.84 m. With these parameters, the maximum dispersion of the ADM section is calculated to be approximately 11 mm, as illustrated in Fig. 3.

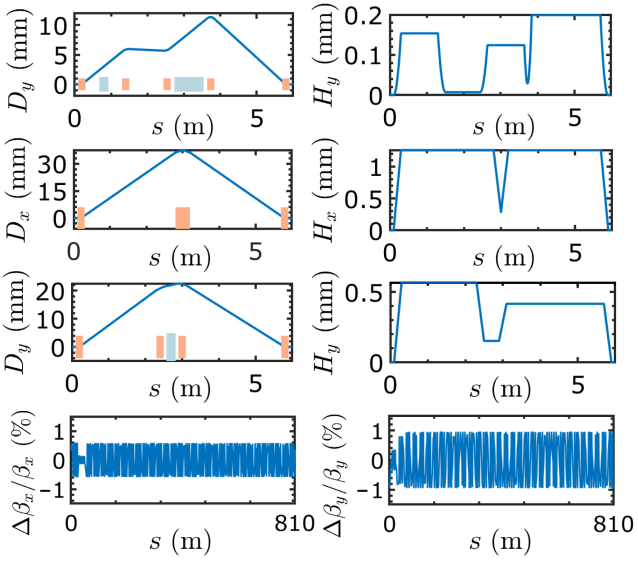


FIG. 3. Dispersion and H-function of the ADM (first row), chicane (second row) and demodulation (third row) sections, and beta-beating of the storage ring (fourth row).

To achieve isochronous transport between the modulation and the demodulation, the chicane parameter θ and the parameters θ_4, θ_5 of the vertical dipoles upstream of the modulator in the demodulation section are set to 13.9, 9.59, and -6.73 mrad, respectively. Other parameters are detailed in the Appendix. These specified parameters result in a horizontal dispersion of 37 mm. Additionally, the demodulation section contributes a vertical dispersion of 22.5 mm, as shown in Fig. 3.

The beta-beating, which represents the change in the beta function between the ring with and without the reversible ADM, is also shown in Fig. 3. The results demonstrate that the beta-beating is smaller than 1%. Importantly, this low beta-beating has only a minimal impact on the overall beta-beating caused by other insertion devices with reasonable errors and misalignments. While such beta-beating could typically be corrected to an acceptable level, we found in our specific case that its impact was negligible. Therefore, we chose not to implement this correction.

After completing the design, we calculated the dynamic aperture (DA) and the local momentum aperture (MA). As shown in Fig. 4, after incorporating the ADM, chicane, and demodulation sections, the DA area decreased by only 10%, with the momentum aperture experiencing the largest reduction in the chicane section, dropping to 4%. However, in the ADM and demodulation sections, the MA remains above 4%. These changes have a negligible impact on the routine operation of the storage ring.

The final emittances are 36.82 pm in the horizontal direction and 1.2 pm in the vertical direction. We adopted the ELEGANT [32] code to implement laser modulation and tracking the modulated beam through the ADM section,

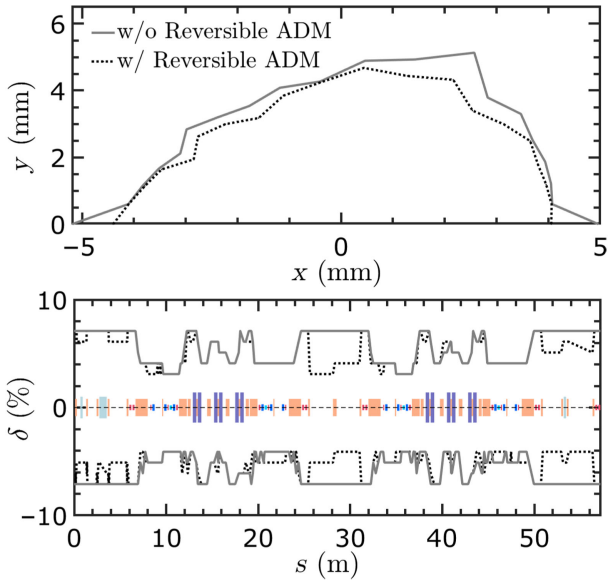


FIG. 4. Dynamic aperture and local momentum aperture for SAPS ring with and without ADM, chicane, and demodulation sections.

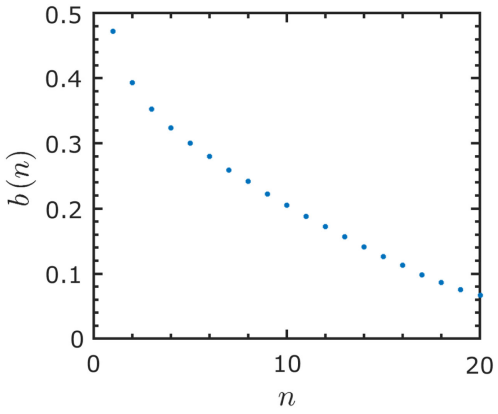


FIG. 5. Bunching factor at different harmonic number.

arc, chicane, and the demodulation section. After the density modulation, the bunching factor versus the harmonic number is illustrated in Fig. 5. It can be observed that the 10th harmonic bunching factor is up to 0.2.

During the demodulation process, perfect synchronization between the modulated and demodulated lasers is assumed. The detailed implementation of the optical path will be explored in future studies. Upon completion of the demodulation, the beam's phase space is effectively restored. This is attributed to the achievement of isochronous transport, as shown in Fig. 6, where from the center of the ADM modulator to the center of the modulator in the demodulation, $R_{5i,\mathrm{tot}} = 0$ $(i = 1, 2, 3, 4, 6)$. When considering only linear terms of the transport and treating the energy modulation as an equivalent sinusoidal point kick, following demodulation, the increases in energy spread and vertical emittance are nearly negligible. However, in a more realistic scenario that accounts for nonlinear terms of the transport, 3D laser-electron beam interaction, and finite-length modulators, the increase in energy spread rises to 0.08%, and the increase in vertical emittance to 16.0%, indicating a significant growth compared to the ideal case. This indicates an influence of nonlinear terms, and further reduction in parameter growth may be achievable by appropriately optimizing the multipole magnets in the arc section. Nevertheless, this would likely compromise the symmetry of the ring and potentially affect its dynamics. Addressing this issue may require alternative strategies and is beyond the scope of this paper. Fortunately, in our case, such optimization is unnecessary.

B. Intrabeam scattering effect and Touschek lifetime

In the previous design, we only considered the case of zero beam current. When a certain beam current is considered, the intrabeam scattering (IBS) effect may become significant, as it further increases the emittance of the storage ring, thereby reducing the bunching factor of the ADM.

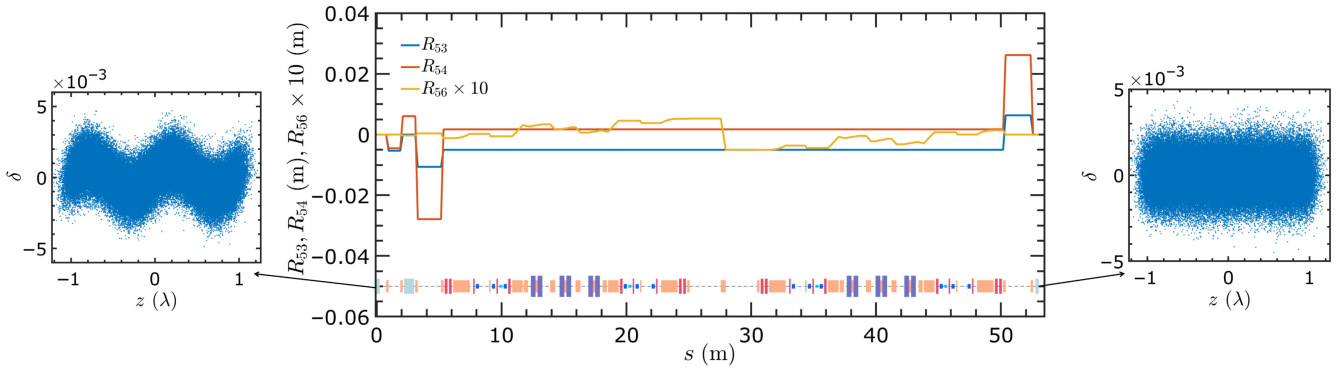


FIG. 6. Transfer matrix terms R_{53}, R_{54}, and R_{56} along the transport line between the center of the modulator and the demodulator.

To analyze the IBS effect, we use Bane's high-energy approximation [33] to calculate the IBS diffusion times T_x, T_y, and T_δ. It is important to note that the vertical emittance has two contributions: one from the vertical dispersion and the other from the coupling of the betatron motion. We define the factor of the betatron coupling as κ_β. Under the assumption of small κ_β, the beam's equilibrium parameters can be derived from the following equations [33]:

$$\begin{aligned}\epsilon_x &= \frac{t_x}{T_x}\epsilon_x + \epsilon_{x0},\\ \epsilon_y &= \kappa_\beta \epsilon_x\left(1-\frac{t_y}{T_y}\right) + \frac{t_y}{T_y}\epsilon_y + \epsilon_{y0,d},\\ \sigma_\delta &= \frac{t_\delta}{T_\delta}\sigma_\delta + \sigma_{\delta 0}.\end{aligned} \tag{6}$$

Here, $t_{x,y,z}$ are the synchrotron radiation damping times, ϵ_{x0} and $\sigma_{\delta 0}$ are the horizontal emittance and energy spread at zero beam current, respectively, and $\epsilon_{y0,d}$ is the vertical emittance due to the vertical dispersion at zero beam current.

We consider the case where the single-bunch charge is 1 nC and the betatron coupling is 0.1%. Such a low coupling level is expected to be achievable through the resonance driving terms correction method [34]. To maintain emittance stability, we aim to limit the coupling variation to no more than 10%, which would keep the jitter of the bunching factor and radiation power within 1%.

We examine three different radiation wavelengths, with harmonic numbers of 8, 9, and 10. These different harmonics can be realized by adjusting the gap of the radiator. The beam parameters for these three cases are provided in Table I.

It is important to note that the emittance differences among these three cases are quite small, indicating that under constant betatron coupling, the effect of undulator focusing on the vertical emittance remains weak within the parameter range shown in Table I. For larger gap variations, additional damping wigglers could be installed in the storage ring to stabilize the emittance [35].

For simplicity and without loss of generality, in the subsequent calculations, we assume the equilibrium emittance after considering IBS to be 103 pm horizontally and 2 pm vertically for all three cases in Table I. The corresponding beam parameters are a bunch length of 3.8 mm, a peak current of 31.5 A, and an energy spread of 0.14%. Under these conditions, after demodulation, the energy spread increases by 0.1%, and the vertical emittance increases by 22%. These results are larger than those for the case without considering IBS, suggesting that the demodulation effect depends on the beam's initial parameters.

Based on the beam parameters above and the MA results provided in Sec. III A, we can estimate the Touschek lifetime of the demodulated beam. We use touschekLifetime tool in ELEGANT, which calculates the Touschek lifetime using Piwinski's formula [36]. The results show that the Touschek lifetime of the demodulated beam is approximately 1.44 h. With this lifetime, to maintain a current stability of 0.1%, a top-up injection mode can be employed, with injections occurring at a repetition rate of 0.1 Hz, which is achievable with current technology.

TABLE I. Emittance for different harmonics with and without IBS.

Parameter	Value		
Harmonic number	8	9	10
Radiator peak field (T)	0.63	0.59	0.54
(ϵ_x, ϵ_y) [pm] no coupling and IBS	(36.84, 1.27)	(36.83, 1.22)	(36.82, 1.20)
(ϵ_x, ϵ_y) [pm] with coupling and IBS	(102.6, 1.95)	(103.2, 1.90)	(103.4, 1.88)

IV. REPETITION RATE AND RADIATION PERFORMANCE

The demodulated beam must complete an adequate number of turns in the storage ring (with the laser off) to restore its quality for the subsequent ADM process (with the laser on). It is crucial to avoid excessive turns, as this would lead to a reduction in the repetition rate. Conversely, if the number of turns is insufficient, the beam quality may fail to recover adequately, resulting in progressively poorer performance in the ensuing ADM processes. In this section, we will simulate and analyze the modulation and demodulation processes, along with the damping process, to determine the optimal number of turns. Based on this optimal outcome, we will also simulate the coherent radiation associated with various ADM processes to demonstrate the radiation performance.

Note that in the following analysis, we consider only the single-bunch dynamics. For multibunch operation, collective effects must be taken into account, which is beyond the scope of this work. We believe that for burst mode, a single-bunch analysis is sufficient.

In the simulation of the ADM process, we employed element-by-element particle tracking in a 3D framework, as described in the previous section, to accurately capture the changes in beam quality after demodulation. However, during the damping process, both the modulation and demodulation lasers are turned off, so we can focus solely on parameter variations at the macrobunch length scale rather than the details at the microbunch scale. To optimize computational efficiency, we simplify the simulation of the damping process as follows.

We track the 4D state coordinates (x, x', y, y') of particles in the ring from turn i to turn $i+1$ using the following one-turn map:

$$\begin{pmatrix} x_{i+1} \\ x'_{i+1} \\ y_{i+1} \\ y'_{i+1} \end{pmatrix} = \begin{bmatrix} \cos\phi_x + \alpha_x \sin\phi_x & \beta_x \sin\phi_x & 0 & 0 \\ -\gamma_x \sin\phi_x & \cos\phi_x - \alpha_x \sin\phi_x & 0 & 0 \\ 0 & 0 & \cos\phi_y + \alpha_y \sin\phi_y & \beta_y \sin\phi_y \\ 0 & 0 & -\gamma_y \sin\phi_y & \cos\phi_y - \alpha_y \sin\phi_y \end{bmatrix} \begin{pmatrix} x_i \\ x'_i \\ y_i \\ y'_i \end{pmatrix}, \tag{7}$$

where $\alpha_{x,y}$, $\beta_{x,y}$, and $\gamma_{x,y}$ are the Twiss parameters, and $\phi_{x,y}$ are the one-turn phase advances, equal to 2π times the working points $\mu_{x,y}$.

The longitudinal state coordinates (z, δ) vary as follows:

$$\begin{aligned} \delta_{i+1} &= \delta_i + \frac{1}{E_0}[eV_c \sin(k_{\mathrm{rf}} z_i + \varphi_s) - U_0], \\ z_{i+1} &= z_i - C_L \alpha_p \delta_{i+1}, \end{aligned} \tag{8}$$

where k_{rf} is the wave number of the rf cavity, C_L is the circumference of the storage ring, α_p is the momentum compaction factor, E_0 is the energy of the storage ring, V_c and φ_s are the rf voltage and synchronous phase, respectively, and U_0 is the one-turn energy loss.

To simulate the effects of synchrotron radiation damping and quantum excitation, we adopt Hirata's method [37], which can be expressed as follows [38,39]. First, we transform the state vector $\mathbf{x} = (x, x', y, y', z, \delta)$ into a normalized state vector $\mathbf{X}$:

$$\mathbf{X} = \mathbf{M}\mathbf{x}. \tag{9}$$

The normalization matrix $\mathbf{M}$ is expressed as

$$\mathbf{M} = \begin{bmatrix} \frac{1}{\sqrt{\beta_x}} & 0 & 0 & 0 & 0 & 0 \\ \frac{\alpha_x}{\sqrt{\beta_x}} & \sqrt{\beta_x} & 0 & 0 & 0 & 0 \\ 0 & 0 & \frac{1}{\sqrt{\beta_y}} & 0 & 0 & 0 \\ 0 & 0 & \frac{\alpha_y}{\sqrt{\beta_y}} & \sqrt{\beta_y} & 0 & 0 \\ 0 & 0 & 0 & 0 & \frac{1}{\sqrt{\beta_z}} & 0 \\ 0 & 0 & 0 & 0 & \frac{\alpha_z}{\sqrt{\beta_z}} & \sqrt{\beta_z} \end{bmatrix}, \tag{10}$$

where α_z and β_z are the longitudinal Twiss parameters. Without loss of generality, we can assume $\alpha_z = 0$ and define β_z as the bunch length divided by the energy spread σ_z/σ_δ.

Thereafter, the effects of synchrotron radiation damping and quantum excitation are simulated using the one-turn map of the normalized vector $\mathbf{X}$:

$$\begin{aligned} \begin{pmatrix} X_1 \\ X_2 \end{pmatrix} &= \lambda_x \begin{pmatrix} X_1 \\ X_2 \end{pmatrix} + \sqrt{\epsilon_x(1-\lambda_x^2)} \begin{pmatrix} r_1 \\ r_2 \end{pmatrix} \\ \begin{pmatrix} X_3 \\ X_4 \end{pmatrix} &= \lambda_y \begin{pmatrix} X_3 \\ X_4 \end{pmatrix} + \sqrt{\epsilon_y(1-\lambda_y^2)} \begin{pmatrix} r_3 \\ r_4 \end{pmatrix} \\ \begin{pmatrix} X_5 \\ X_6 \end{pmatrix} &= \begin{pmatrix} 1 & 0 \\ 0 & \lambda_z^2 \end{pmatrix} \begin{pmatrix} X_5 \\ X_6 \end{pmatrix} + \sqrt{\epsilon_z(1-\lambda_z^4)} \begin{pmatrix} 0 \\ r_6 \end{pmatrix} \end{aligned}. \tag{11}$$

Here, the vector $\mathbf{r} = (r_1, r_2, r_3, r_4, 0, r_6)$ represents a five-dimensional independent Gaussian random variable.

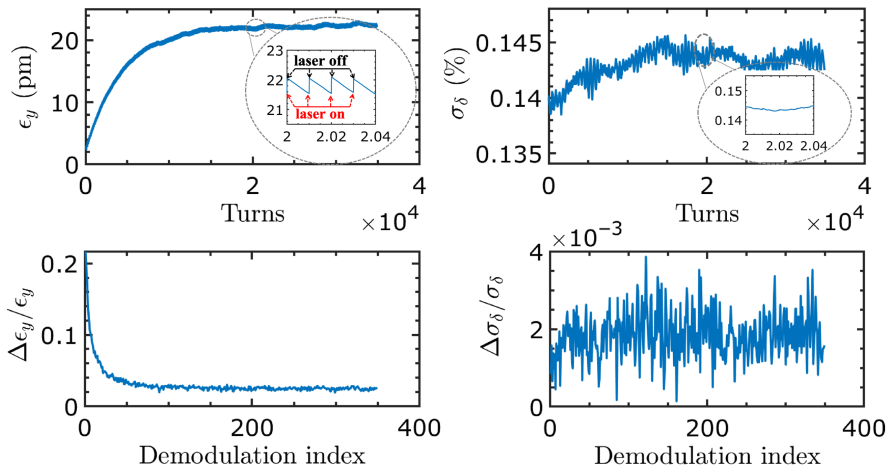


FIG. 7. Variation in vertical emittance and energy spread with turns during damping and ADM processes, alongside corresponding growth rates following each demodulation.

The damping coefficients $\lambda_{x,y,z} = \exp(-1/\tau_{x,y,z})$, where $\tau_{x,y,z}$ are the synchrotron radiation damping times measured in terms of the revolution time. The parameters $\epsilon_{x,y,z}$ denote the equilibrium emittance, with $\epsilon_z = \sigma_z\sigma_\delta$.

Finally, the state vector $\mathbf{x}$ after damping and quantum excitation can be obtained by applying the inverse normalization matrix:

$$\mathbf{x} = \mathbf{M}^{-1}\mathbf{X}. \tag{12}$$

To develop a comprehensive understanding of beam parameter evolution as a function of the number of turns N, we set $N = 100$ as an example, indicating that the ADM process is conducted after every 100 damping turns. The resulting variations in beam parameters are illustrated in Fig. 7. These results demonstrate that the vertical emittance stabilizes at approximately 22 pm after around 20,000 turns, with periodic increases occurring at each 100-turn interval. The growth rate of emittance following demodulation reaches stability after approximately 100 ADM process cycles (around 10,000 turns). In contrast, the energy spread remains largely unaffected by the demodulation process, with variations primarily driven by longitudinal motion and quantum excitation, leading to

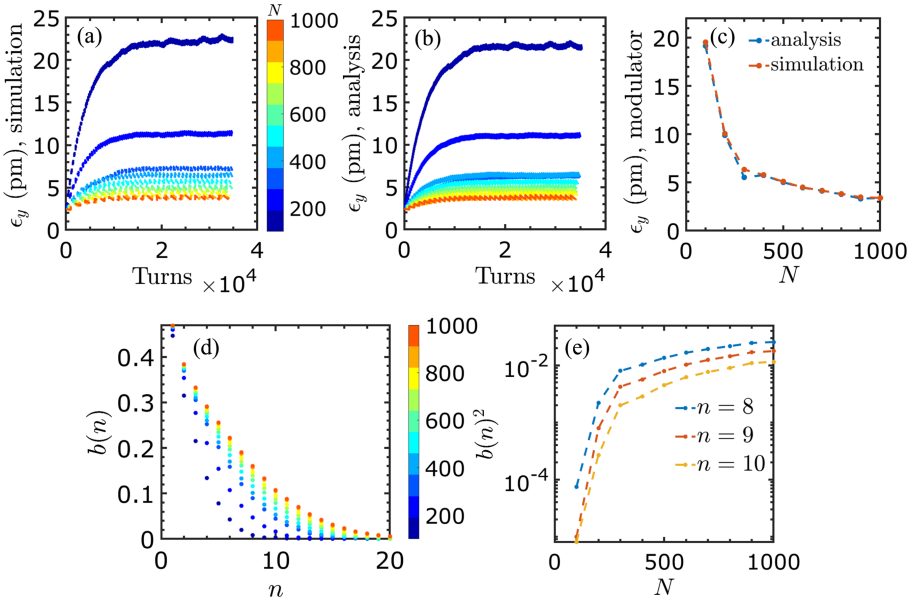


FIG. 8. Variation of vertical emittance with turns under different N: (a) simulation results, (b) analytical results, (c) stable emittance at the ADM modulator entrance under different N, (d) bunching factor at approximately 35,000 turns across different N and harmonic numbers, and (e) variation of the squared bunching factor with N at the target harmonic number. It is noteworthy that the fluctuations observed in the curves of (a) and (b) exhibit similar patterns, which is likely due to the use of the simulated results from each demodulation as the initial parameters for the emittance calculations using Eq. (13).

fluctuations of less than 0.4%. Given the negligible impact of these fluctuations in energy spread on the ADM process, we will focus exclusively on presenting and analyzing the changes in vertical emittance in the subsequent analysis, while acknowledging that variations in energy spread are included in the calculations but will not be explicitly discussed.

To determine the optimal number of turns N, we conducted a detailed analysis of vertical emittance variations across different N. The findings are presented in Fig. 8, which illustrates a decrease in stable emittance as N increases. Notably, when N is below 300, the emittance exhibits considerable variation; however, for N exceeding 300, the changes become relatively minor. By examining the relationship between the bunching factor and its square (which is proportional to radiation power) as a function of N, it becomes apparent that further increasing N beyond 600 yields only marginal improvements in radiation power.

To benchmark these results, we employed the theoretical formula for emittance variation over time under laser-off conditions [27]:

$$\epsilon_y(t) = \epsilon_y(0)e^{-2t/\tau_y} + \epsilon_{y0}(1 - e^{-2t/\tau_y}). \tag{13}$$

Here, $\epsilon_y(0)$ represents the emittance after demodulation obtained from ELEGANT simulations of the ADM process, while ϵ_{y0} denotes the equilibrium emittance in the vertical direction, which is 2 pm.

Using Eq. (13), we calculated the emittance after N turns. As shown in Fig. 8, the results demonstrate a good agreement between theoretical predictions and numerical simulations.

We take the optimal N as 600, meaning that the ADM process is performed approximately every 1.62 ms. Considering that the storage ring contains 450 buckets with a 90% filling pattern, the SAPS reversible ADM can achieve a maximum repetition rate of approximately 0.25 MHz.

Notably, after the beam stabilizes around 11,000 turns, small differences in beam parameters persist at the modulation entrance, despite the overall stability. These discrepancies can lead to variations in the bunching factor, which, in turn, affect radiation performance. To assess the significance of these differences, we calculated the radiation pulses during the ADM process from turns 11,000 to 35,000. Starting at turn 11,000, the laser was activated every 600 turns when the beam entered the ADM section. Following modulation with a laser of 700 fs duration, the beam passing through the radiator generated coherent radiation. A total of 40 radiation were simulated using the GENESIS code [40], with each pulse generated every 600 turns.

As shown in Fig. 9, the duration of these radiation pulses is approximately 1 ps and the photon number per pulse is approaching 7×10^9 for a radiation pulse with a wavelength of 33.25 nm, exhibiting an approximately 6% variation among different pulses. Considering a repetition rate of 0.25 MHz, the average flux reaches 1.8×10^{15} photons/s. The bandwidth of the radiation pulses is approximately 2.5 meV, with variations remaining below 1.3%. The performance for other radiation wavelengths is also shown in Fig. 9.

For comparison, we estimated the photon flux produced by three 6-m-long undulators under equivalent bandwidth conditions to be around 2.5×10^{13} photons/s. Although this estimation may be higher than the actual photon flux, it still falls beyond 1 order of magnitude lower than that of coherent radiation.

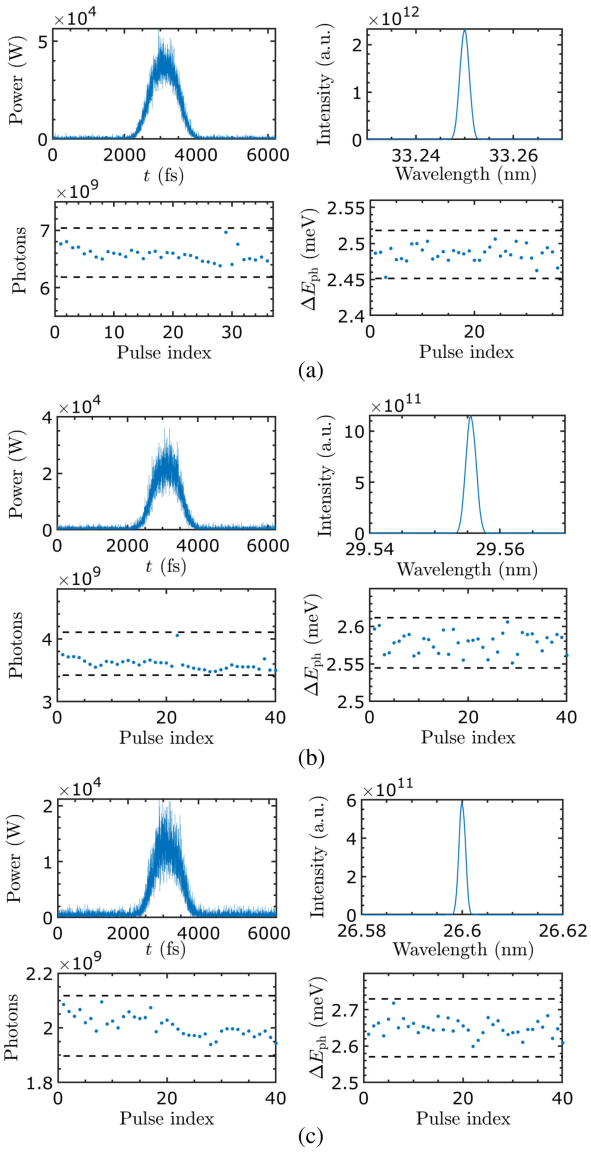


FIG. 9. Radiation pulse and spectrum for a single ADM process, including pulse-by-pulse variations in photon number and bandwidth across multiple ADM processes. Panels (a)–(c) show the results for different radiation wavelengths.

V. DISCUSSION AND CONCLUSION

We propose an easy-to-implement method to achieve reversible laser modulation in storage rings. This scheme utilizes two arcs and three straight sections of the storage ring. By incorporating a chicane within one of the straight sections, an isochronous transfer from the modulation section to the demodulation section is achieved, thereby eliminating energy modulation. Based on the SAPS parameters, we present a design. The results indicate that after beam modulation, a large bunching factor can be achieved at the high harmonic. Under modulation by a laser with several hundred femtoseconds duration, picoseconds radiation pulse can be achieved with large average flux.

After demodulation, the beam parameters are largely recovered. However, compared to the case under ideal conditions, the beam energy spread and vertical emittance increase significantly. This difference is attributed to higher-order effects in the transport process. Future efforts will focus on reducing this discrepancy by locally optimizing the nonlinear elements in the arcs. At the current growth rate, beam recovery requires approximately 1.62 μs, allowing for a repetition rate of up to 0.25 MHz.

It is noteworthy that the reversible ADM has some effects on the storage ring dynamics. Since the longitudinal dispersion of the transport between modulation and demodulation is zero, the momentum compaction factor of the whole ring will be reduced. This reduction will have some effect on the longitudinal dynamics, although in our case the momentum compaction factor is only reduced by $2/32 \sim 6\%$ due to the multiple periods of the SAPS, and the effect on the longitudinal dynamics is negligible. For storage rings with a few periods, e.g., only two periods, this effect is significant. For this kind of storage ring design, steady-state microbunching storage ring-related studies can be used as a guide [41,42].

In addition, the scheme utilizes three straight sections, which presents a clear disadvantage in terms of beamline utilization. This drawback could be addressed by designing a storage ring with longer straight sections, thereby enabling the scheme to be implemented with only two straight sections. Alternatively, longitudinal dispersion of the chicane could be achieved by utilizing the horizontal components of the dipoles in the ADM and demodulation sections, although this approach may increase the complexity of mechanical alignment. Further research into more effective solutions to this challenge is warranted.

In this study, the modulator and demodulator lasers are assumed to be perfectly synchronized. If there is a phase error between the two lasers, the beam would require additional damping turns to restore its parameters. If the requirement is to limit the increase in damping turns to no more than a factor of two, preliminary estimates suggest that the phase error must be kept below 1/50 of the modulator laser wavelength. Achieving such small phase errors is challenging and requires precise phase control techniques [43,44]. Considering other requirements for our laser systems, more detailed studies and technical evaluations will be conducted in future work.

Nevertheless, we have not addressed the specific implementation of laser-beam synchronization. Currently, synchronization between the storage ring electron beams and lasers can achieve jitter on the order of a few ps [45]. For electron beams with bunch lengths of several hundred ps, this level of jitter is sufficient. However, for shorter bunch lengths on the order of a few ps, we aim to reduce jitter to the tens of fs level. This is potentially achievable, as fs-level jitter has already been demonstrated in FELs [46]. Future research that integrates FEL-related technologies for laser-beam synchronization in storage rings could help achieve this goal.

ACKNOWLEDGMENTS

This work was supported by the National Natural Science Foundation of China (No. 12405176, No. 12275284, and No. 11922512), and Youth Innovation Promotion Association of the Chinese Academy of Sciences (No. Y201904).

APPENDIX: PARAMETERS TABLE OF THE REVERSIBLE ADM

For convenience, we have compiled the parameters used throughout this paper in Table II below.

TABLE II. Parameters of the reversible ADM.

Parameter	Value	Unit
	Ring	
C_L	810	m
α_p	2.334×10^{-5}	
U_0	0.921	MeV
V_c	3.00	MV
μ_x, μ_y	(7.6123, 4.9091)	
β_x, β_y	(6.75, 6.41)	m
α_x, α_y	(0.613, 0.6657)	
k_{rf}	3.49	1/m
$R_{56,r}$	0.638	mm
Damping time (t_x, t_y, t_δ)	13.70, 20.50, 13.60	ms
Peak current	31.50	A
	ADM section	
Dipole		
Bending angle	5.00	mrad
Length	0.20	m
Dogleg		
Bending angle	5.31	mrad
Length	0.20	m
Distance between dipoles	0.94	m
Modulator		
Peak field	0.60	T

(Table continued)

TABLE II. *(Continued)*

Parameter	Value	Unit
Period	0.25	m
Period number	1	
Radiator		
Peak field	0.54	T
Period	0.12	m
Period number	7	
Laser		
Peak power	62.4	GW
Waist size	0.14	mm
Duration	700	fs
Chicane		
Dipole angle	13.91	mrad
Dipole length	0.20	m
Distance between first and second dipoles	2.50	m
Demodulation section		
First dipole length	0.20	m
First dipole angle	9.59	mrad
Second dipole length	0.20	m
Second dipole angle	−6.73	mrad
Distance between first and second dipole	2.00	m
Third dipole length	0.20	m
Third dipole angle	−11.01	mrad
Distance between second and third dipole	0.40	m
Fourth dipole length	0.20	m
Fourth dipole angle	8.15	mrad
Distance between third and fourth dipole	2.60	m

[1] W. Decking, S. Abeghyan, P. Abramian *et al.*, A MHz-repetition-rate hard X-ray free-electron laser driven by a superconducting linear accelerator, Nat. Photonics **14**, 391 (2020).

[2] J. Duris, S. Li, T. Driver *et al.*, Tunable isolated attosecond X-ray pulses with gigawatt peak power from a free-electron laser, Nat. Photonics **14**, 30 (2020).

[3] J. Li and Y. Liu, Hearing the heartbeat of atoms: Unveiling attosecond horizons, Ultrafast Sci. **3**, 0049 (2023).

[4] D. Einfeld, M. Plesko, and J. Schaper, First multi-bend achromat lattice consideration, J. Synchrotron Radiat. **21**, 856 (2014).

[5] B. Girard, Y. Lapierre, J. M. Ortega *et al.*, Optical frequency multiplication by an optical klystron, Phys. Rev. Lett. **53**, 2405 (1984).

[6] G. De Ninno, E. Allaria, and M. Coreno *et al.*, Generation of ultrashort coherent vacuum ultraviolet pulses using electron storage rings: A new bright light source for experiments, Phys. Rev. Lett. **101**, 053902 (2008).

[7] C. Evain, A. Loulergue, A. Nadji, J. M. Filhol, M. E. Couprie, and A. A. Zholents, Soft x-ray femtosecond coherent undulator radiation in a storage ring, New J. Phys. **14**, 023003 (2012).

[8] W.-H. Liu, G.-Q. Zhou, and Y. Jiao, Generating femtosecond coherent X-ray pulses in a diffraction-limited storage ring with the echo-enabled harmonic generation scheme, Nucl. Sci. Tech. **29**, 143 (2018).

[9] X. Yang, G. Penn, L. H. Yu, V. Smaluk, and T. Shaftan, Optimization of echo-enabled harmonic generation toward coherent EUV and soft X-ray free-electron laser at NSLS-II, Sci. Rep. **12**, 9437 (2022).

[10] J.-G. Hwang, G. Schiwietz, M. Abo-Bakr, T. Atkinson, M. Ries, P. Goslawski, G. Klemz, R. Müller, A. Schälicke, and A. Jankowiak, Generation of intense and coherent sub-femtosecond X-ray pulses in electron storage rings, Sci. Rep. **10**, 10093 (2020).

[11] A. A. Zholents and M. S. Zolotorev, Attosecond x-ray pulses produced by ultra short transverse slicing via laser electron beam interaction, New J. Phys. **10**, 025005 (2008).

[12] D. Xiang and W. Wan, Generating ultrashort coherent soft X-ray radiation in storage rings using angular-modulated electron beams, Phys. Rev. Lett. **104**, 084803 (2010).

[13] X. Wang, C. Feng, T. Liu, Z. Zhang, C.-Y. Tsai, J. Wu, C. Yang, and Z. Zhao, Angular dispersion enhanced prebunch for seeding ultrashort and coherent EUV and soft X-ray free-electron laser in storage rings, J. Synchrotron Radiat. **26**, 677 (2019).

[14] Y. Lu, X. Wang, X. Deng, C. Feng, and D. Wang, Methods for enhancing the steady-state microbunching in storage rings, Results Phys. **40**, 105849 (2022).

[15] C. Feng and Z. Zhao, A storage ring based free-electron laser for generating ultrashort coherent EUV and X-ray radiation, Sci. Rep. **7**, 4724 (2017).

[16] C. Li, C. Feng, and B. Jiang, Extremely bright coherent synchrotron radiation production in a diffraction-limited storage ring using an angular dispersion-induced microbunching scheme, Phys. Rev. Accel. Beams **23**, 110701 (2020).

[17] W. Liu, Y. Zhao, Y. Jiao, and S. Wang, Generating high repetition rate X-ray attosecond pulses in a diffraction limited storage ring, Sci. Rep. **13**, 14019 (2023).

[18] B. Jiang, C. Feng, C. Li, Z. Bai, W. Wan, D. Xiang, Q. Gu, K. Wang, Q. Zhang, D. Huang, and S. Chen, A synchrotron-based kilowatt-level radiation source for EUV lithography, Sci. Rep. **12**, 3325 (2022).

[19] Z. Li, X. Deng, Z. Pan, C. Tang, and A. Chao, Generalized longitudinal strong focusing in a steady-state microbunching storage ring, Phys. Rev. Accel. Beams **26**, 110701 (2023).

[20] J. B. Murphy and C. Pellegrini, Free electron lasers for the XUV spectral region, Nucl. Instrum. Methods Phys. Res., Sect. A **237**, 159 (1985).

[21] K.-J. Kim, J. Bisognano, A. Garren, K. Halbach, and J. Peterson, Issues in storage-ring design for operation of high-gain FEL, Nucl. Instrum. Methods Phys. Res., Sect. A **239**, 54 (1985).

[22] H.-D. Nuhn, R. Tatchyn, H. Winick, A. S. Fisher, J. C. Gallardo, and C. Pellegrini, Short wavelength FELs on large storage rings, Nucl. Instrum. Methods Phys. Res., Sect. A **319**, 89 (1992).

[23] R. R. Lindberg, Y. Cai, K.-J. Kim, and Z. Huang, Transverse gradient undulators for a storage ring-based X-ray FEL oscillator, in *Proceedings of the 35th International Free-Electron Laser Conference*, edited by C. Scholl and V. Schaa (JACoW, New York, NY, 2013), THOBNO02.

[24] Y. Cai, Y. Ding, R. Hettel, Z. Huang, L. Wang, and L. X. and, An X-ray free electron laser driven by an ultimate storage ring, Synchrotron Radiat. News **26**, 39 (2013).

[25] S. D. Mitri and M. Cornacchia, Operating synchrotron light sources with a high gain free electron laser, New J. Phys. **17**, 113006 (2015).

[26] Z. Huang, K. Bane, Y. Cai, A. Chao, R. Hettel, and C. Pellegrini, Steady-state analysis of short-wavelength, high-gain FELs in a large storage ring, Nucl. Instrum. Methods Phys. Res., Sect. A **593**, 120 (2008).

[27] S. Di Mitri, M. Cornacchia, B. Diviacco, G. Perosa, F. Sottocorona, and S. Spampinati, Bridging the gap of storage ring light sources and linac-driven free-electron lasers, Phys. Rev. Accel. Beams **24**, 060702 (2021).

[28] Y. Zhao, Y. Jiao, and S. Wang, Design study of APS-U-type hybrid-MBA lattice for mid-energy DLSR, Nucl. Sci. Tech. **32**, 71 (2021).

[29] F. Zeng, Y. Jiao, W. Liu, and C.-Y. Tsai, An asymmetric four-bend S-chicane compressor immune to coherent synchrotron radiation effects, arXiv:2403.06101.

[30] Q. Fu, N. Hanrahan, L. Xu, S. Lane, D. Lin, Y. Jung, S. Mahajan, and D. J. Richardson, High-power, high-efficiency, all-fiberized-laser-pumped, 260-nm, deep-UV laser for bacterial deactivation, Opt. Express **29**, 42485 (2021).

[31] M. Müller, C. Aleshire, A. Klenke, E. Haddad, F. Légaré, A. Tünnermann, and J. Limpert, 10.4 kW coherently combined ultrafast fiber laser, Opt. Lett. **45**, 3083 (2020).

[32] M. Borland, ELEGANT: A flexible SDDS-compliant code for accelerator simulation, Technical Report No. LS-287, 2000. 10.2172/761286

[33] K. L. F. Bane, H. Hayano, K. Kubo, T. Naito, T. Okugi, and J. Urakawa, Intrabeam scattering analysis of measurements at KEK's Accelerator Test Facility damping ring, Phys. Rev. ST Accel. Beams **5**, 084403 (2002).

[34] A. Franchi, L. Farvacque, J. Chavanne, F. Ewald, B. Nash, K. Scheidt, and R. Tomás, Vertical emittance reduction and preservation in electron storage rings via resonance driving terms correction, Phys. Rev. ST Accel. Beams **14**, 034002 (2011).

[35] L. Tan, S. Tian, X. Liu, W. Zhang, X. Wu, and Y. Gong, Emittance and energy spread compensation in future synchrotron light sources, Nucl. Instrum. Methods Phys. Res., Sect. A **1052**, 168278 (2023).

[36] A. Piwinski, The Touschek effect in strong focusing storage rings, arXiv:physics/9903034.

[37] K. Hirata, BBC user's guide: A computer code for beam-beam interaction with a crossing angle, version 3.4, CERN Technical Report No. CERN SL Note 97-57 AP, 1997.

[38] Y. Zhang, K. Ohmi, and L. Chen, Simulation study of beam-beam effects, Phys. Rev. ST Accel. Beams **8**, 074402 (2005).

[39] C. Li and Y.-C. Chae, CETASim: A numerical tool for beam collective effect study in storage rings, Nucl. Instrum. Methods Phys. Res., Sect. A **1070**, 170031 (2025).

[40] S. Reiche, GENESIS 1.3: A fully 3D time-dependent FEL simulation code, Nucl. Instrum. Methods Phys. Res., Sect. A **429**, 243 (1999).

[41] X. Deng, A. Chao, J. Feikes, A. Hoehl *et al.*, Experimental demonstration of the mechanism of steady-state micro-bunching, Nature (London) **590**, 576 (2021).

[42] X. Deng, Steady-state micro-bunching based on transverse-longitudinal coupling, arXiv:2404.06920.

[43] R. Liu, C. Peng, X. Liang, and R. Li, Coherent beam combination far-field measuring method based on amplitude modulation and deep learning, Chin. Optic. Lett. **18**, 041402 (2020).

[44] J. Long, R. Su, T. Hou, Q. Chang, M. Jiang, H. Chang, Y. Deng, Y. Ma, P. Ma, and P. Zhou, System design for coherent combined massive fiber laser array based on cascaded internal phase control, Appl. Opt. **61**, 10222 (2022).

[45] Y. Tanaka, T. Hara, H. Kitamura, and T. Ishikawa, Timing control of an intense picosecond pulse laser to the SPring-8 synchrotron radiation pulses, Rev. Sci. Instrum. **71**, 1268 (2000).

[46] M. B. Danailov, F. Bencivenga, F. Capotondi, F. Casolari, P. Cinquegrana, A. Demidovich, E. Giangrisostomi, M. P. Kiskinova, G. Kurdi, M. Manfredda, C. Masciovecchio, R. Mincigrucci, I. P. Nikolov, E. Pedersoli, E. Principi, and P. Sigalotti, Towards jitter-free pump-probe measurements at seeded free electron laser facilities, Opt. Express **22**, 12869 (2014).